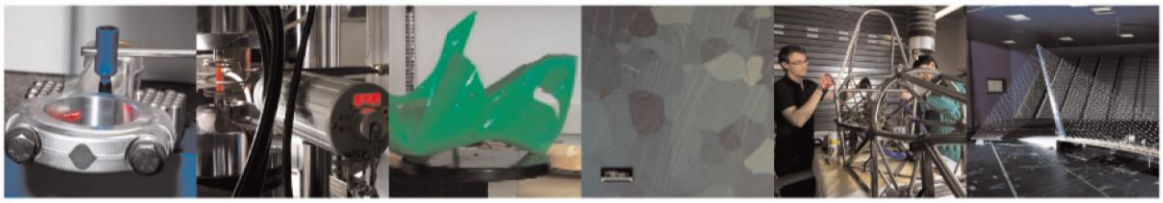

Evolution of Porosity and Geometrical Quality through the Ceramic Extrusion Additive Manufacturing Process Stages

Rane, Kedarnath; Petro', Stefano; Strano, Matteo

DIPARTIMENTO DI MECCANICA ■ POLITECNICO DI MILANO
via G. La Masa, 1 ■ 20156 Milano ■ EMAIL (PEC): pecmecc@cert.polimi.it
http://www.mecc.polimi.it
Rev. 0

Evolution of Porosity and Geometrical Quality through the Ceramic Extrusion Additive Manufacturing Process Stages

Kedarnath Rane*, Stefano Petrò, Matteo Strano

Dipartimento di Meccanica, Politecnico di Milano, Via La Masa 1, Milano, Italy

**Corresponding author- Tel: +39-0223998520, E-mail: Kedarnath.rane@polimi.it*

Abstract

Ceramic Extrusion Additive Manufacturing (CEAM) enables the die-less fabrication of small ceramic parts, with a process chain that includes four consecutive stages: the 3D printing, solvent de-binding, thermal de-binding, and sintering. The 3D printing process was implemented through *Ephestus*, a specially developed EAM machine for the manufacturing of parts from alumina feedstock. A test part was designed, and X-ray computed tomography (μ-CT) was used to quantify its characteristics through the processing stages of the EAM. The porosity distribution and the distribution of void size and shape were determined throughout the samples at each stage, using image analysis techniques. Furthermore, the evolution of some macroscopic quality properties was measured.

The results show that both microscopic (porosity) and macroscopic (geometry, density) properties of the samples improve through the process stages. A vertical gradient of porosity is present in green and de-bound samples, with porosity decreasing with increasing sample height. After sintering, the vertical gradient of porosity disappears. The sphericity and the diameter of voids are negatively correlated and dispersed over a wide range in the green state. The sintering process has a homogenization effect on the void shape distribution. The geometrical deviation from the nominal designed dimensions and the surface quality of parts improves when moving from the green to the sintered state.

Keywords: *material extrusion; feedstock; alumina; porosity mapping; X-ray computed tomography.*

1. Introduction

Stereolithography (SLA) [1] or digital light processing (DLP) [2], powder bed fusion [3] and binder jetting [4] are recognized as the most common Additive Manufacturing (AM) methods for ceramics. The technology of Ceramic Extrusion Additive Manufacturing (CEAM) is growing because it is considered to be an affordable and rapid alternative to the other AM

methods [5]. One of the key advantages of the material extrusion AM technology is its versatility, because it is suited to a wide range of materials, including metals and ceramics [6], and because the process can easily incorporate material removal stages [7].

The CEAM process adapts the typical Ceramic Injection Moulding (CIM) process by replacing the conventional injection moulding stage with a 3D printing stage by extrusion. Both the CIM and the CEAM feedstock are made of a ceramic ultrafine powder, homogeneously mixed with a limited amount (usually less than 50% by volume) of binder compound [8]. The feedstock is extruded in a controlled manner and deposited according to a designed path, to obtain a 3D printed part [9], which is called "green". The post-processing stages in CEAM are similar to the traditional ceramic manufacturing processes by Powder Metallurgy (PM), where a soluble binder is pre-mixed to the material feedstock [10]. Hence, CEAM can considerably benefit from the existing know-how of an established ceramics community. During post-processing, binders are removed in two stages: first a solvent (or catalytic) binder removal operation is performed to remove approximately half of the binder mass; then, a thermal binder removal treatment is performed inside a furnace [11]. A porous "brown" structure of powder is formed thereafter [12]. The brown part is finally sintered to achieve the desired geometry, density and mechanical strength. In some case, the CEAM process can be implemented with a low viscous slurry compound, that does not require the intermediate binder removal steps before sintering [13].

Although the CEAM processes can produce relatively complex geometries, this advantage is significantly compromised by a lack of microstructural quality control within the ceramic parts. In fact, various issues concerning porosity, purity, micro-defects and interfacial defects commonly affect EAM ceramic structures [14,15]. Furthermore, due to the staircase effect, which is inherent to all AM processes, dimensional accuracy, and surface quality are poor, and notch sensitivity of the printed ceramic parts is critical [16].

Porosity in EAM parts is partly due to the volume filling capability of the green 3D printing process. The effect of porosity in the green parts is due to the 3D printing parameters, and it is described by some (limited) available literature on the conventional EAM of polymers. As an example, in [17], the authors study the influence of print parameters on the porosity of on a polyetherimide polymer. Some previous study is also available for CEAM, but they focus on the evolution of extruded porous ceramic structures, where the porosity is large, intended and controlled [18,19]. However, in structural applications, porosity is a defect and must be avoided.

Porosity is also sensitive to the subsequent post-processing (de-binding and sintering) stages. It has been investigated by some authors for conventional CIM processes, but no study has been performed on its gradient inside a single part. In [20], the authors show that, after thermal de-binding, the average final void size is proportional to the de-binding temperature. Sintering is a bulk volumetric diffusion phenomenon and induces shrinkage, approximately isotropic but influenced considerably by sintering time and temperature [21]. On the contrary, after sintering it has been demonstrated that porosity increases if reducing the sintering temperature of bi-material ceramic parts [22]. An interesting and relevant study is given in [23], where the authors observe the porosity of porous ceramic samples during and after sintering. They show how larger voids (around 40 μm in size) gets smaller during the cycle.

There is nearly no published scientific literature on the evolution of porosity through the CEAM process. As one of the very few examples, Iyer et al. [24] present the green and sintered properties of Si3N4, such as part shrinkage and warping, microstructural characteristics, by using optical microscopy, scanning electron microscopy, and X-ray diffraction.

The purpose of the present paper is to fill this void in the scientific literature, by presenting a quantitative porosity analysis of the distribution, shape, and size of voids through the whole process chain, from 3D printing to solvent de-binding, and finally sintering. The overall process parameters have been described during 3D printing, de-binding and sintering and all have been kept constant throughout the study. The present study therefore only clarifies how the distribution and the morphology of voids evolve inside a given geometry.

In Section 1.1, a brief overview is given on the porosity evaluation techniques by image processing. In Section 2, the experimental conditions and methods are described. In section 3.1, overall density measurements are presented and discussed. Sections 3.2 to 3.5 focus on the porosity characterization. Sections 3.6 and 3.7 deal with dimensional and surface quality of samples.

1.1 Porosity assessment techniques by image analysis

The major techniques used to measure porosity are the helium pycnometer and the analysis of microscopic images [25]. Image analysis is best suited to the present study because it can provide a geometrical distribution of the defects. There are multiple methods to obtain the necessary images for porosity analysis. In the present study, X-ray micro-computed

tomography (μ-CT) is used because of its capability of non-destructively inspecting internal structures. Multiple μ-CT images have been frequently used for the analysis of porous products, such as metal foams or AM parts produced by SLM [26] or SLS [27]. Though the μ-CT image analysis method usually involves time-consuming scans and complex analysis procedures [28], it provides highly informative results. However, it must be recognized that the technique inherently has a notable dependence on the voxel size, which is a non-trivial factor affecting the quantitative porosity characterization analysis [29]. Thus, it must be acknowledged that the measurements and results are approximations which are not necessarily indicative of "absolute" values but indicate trends within a given application. Furthermore, a key requirement for porosity measurement based on image analysis is to find a proper threshold for transforming original into binary images to distinguish voids from solid material, be it the polymeric binder or the powder particles. There are several methods implemented for thresholding, i.e. converting greyscale images to monochrome. Otsu's method is one of the most common techniques for thresholding [30]. Otsu's method iterates among possible threshold values until it finds the threshold where the sum of foreground and background spreads is minimum. The method had already been successfully used by the authors for the measurement of voids inside samples of porous metals [31]; it has been used already for analysis of μ-CT images of 3D printed parts [32].

2. Materials and methods

A test artefact is used, made of two cylindrical regions, one on top of the other, aligned with their vertical axis, respectively with diameters 8 and 4 mm for the lower and the upper cylinders. A total of 16 samples were produced, and four samples for each stage were taken for porosity analysis. 4 samples for each processing stage have been produced by CEAM with identical printing and processing conditions, in order to take process variability into account. The porosity and the geometrical characteristics of samples were assessed mainly by means of X-ray microtomographic measurements. The thermally de-bound parts were too fragile and too difficult to handle in tomographic measurement operations. Hence, the porosity of parts at the thermally de-bound stage was not analysed. As follows, the material properties, the processing conditions, and the measurement variables and setups are described.

2.1 Feedstock Material

A commercial feedstock provided by Inmatec was used as the raw material, based on a polyolefin binder system, loaded with alumina powder at 60 vol. %, with a median particle size (D_{50}) of 2 µm. The theoretical full density of the solid fraction of the feedstock is 3.92 g/cm³. The typical nominal linear shrinkage after sintering of the injection moulded parts is 15.5 % (mould factor 1.18). The chemical composition of the powder is given in Table 1.

Table 1: Chemical composition of the alumina powder used in the present study

Phases	Na_2O	MgO	CaO	Fe_2O_3	SiO_2	Al_2O_3
Wt. %	0.1%	0.9%	1.3%	0.03%	1.8%	96%

2.2 CEAM equipment

An Extrusion based Additive Manufacturing (EAM) system (Ephestus), developed at Politecnico di Milano, was used for 3D printing the alumina parts. The system, previously described in [33], includes a piston-based vertical extrusion unit with no degrees of freedom (DOFs), a robotic deposition table with 3 DOFs and a control panel. On top of the deposition table, a heated plate (200x200 mm) is mounted, that can be set from 40 °C to 90 °C. The extrusion unit can provide up to 25 MPa of pressure in the barrel, allowing to extrude highly viscous feedstock mixtures. The extruder can be equipped with exit nozzles with a diameter of d_n=0.4 mm or higher. The deposition table is actuated by a parallel kinematics robotic design (an inverse linear delta), which avoids inertial vibrations of the unit that might occur during the rapid change of direction during deposition. The machine can easily synchronize and change the filament extrusion velocity at the nozzle, the horizontal table velocity, and the vertical layer height.

The deposition trajectories can be planned with any commercial slicer or, to test non-conventional strategies, with a specially developed Matlab® code. The trajectories are exported to a g-code in cartesian coordinates. The g-code is then translated by the machine controller into a motion plan for each of the 3 axes of the delta table.

2.3 Experimental conditions

In the present work, 16 samples were 3D printed with identical printing parameters, to study the porosity at different states. Four samples were analysed after 3D printing (green state), four samples after solvent binder removal, four samples after thermal binder removal (brown state) and four samples after sintering. Brown parts were highly fragile and used only for

qualitative analysis and density measurements. The other 12 samples were used for porosity determination. The samples were cylindrical pins with a double diameter, as shown in Figure 1 (a). The bottom cylinder has a nominal printed diameter of 8 mm (at the green stage), and a height of 5 mm; the top cylinder has a nominal printed diameter of 4 mm and a height of 5 mm. In figure 1 (b) the extruded roads are shown, and it must be observed that samples are very small, and the number of roads is limited. The main reason to keep the parts small is to allow enough resolution in the microtomographic imaging. Although the total number of layers and roads is limited, the number of voids along each direction inside the samples is large, as the microscopic images reveal, enough to have a representative indication of voids and porosities.

This test shape was designed to study the effect of geometrical discontinuities within a part. In fact, the top and bottom cylinders have different geometrical moduli (volume-to-surface ratio), which might induce a different behaviour while removing the binder and sintering. Besides, the transition between the bottom and top pins might induce a geometrical discontinuity on the porosity distribution.

Starting from the CAD file in STL file format, a G-code was prepared using the Slic3r software. Typically, 3D printed parts have one or two outer contour roads, aimed at improving the surface quality and dimensions, which surround an internal infill. The theoretical infill density was 100%, the extrusion nozzle temperature was 145 °C, the heated plate was set at 80 °C, the table deposition speed was 10 mm/s, the layer height was 0.2 mm. The infill printing strategy was with parallel roads, as shown in Figure 1 (b). In conventional EAM of polymers, the porosity in the infill 3D printed parts is due to the empty space left between adjacent parallel roads on the same layer and between two consecutive layers. Additional porosity is generated at the interface between the infill and the contour. In this study, the μ-CT images have been centred at the core of the samples, in order to capture the porosity generated by the infill only. Therefore, to better to isolate the behaviour of the internal infill roads, no outer contour road was added.

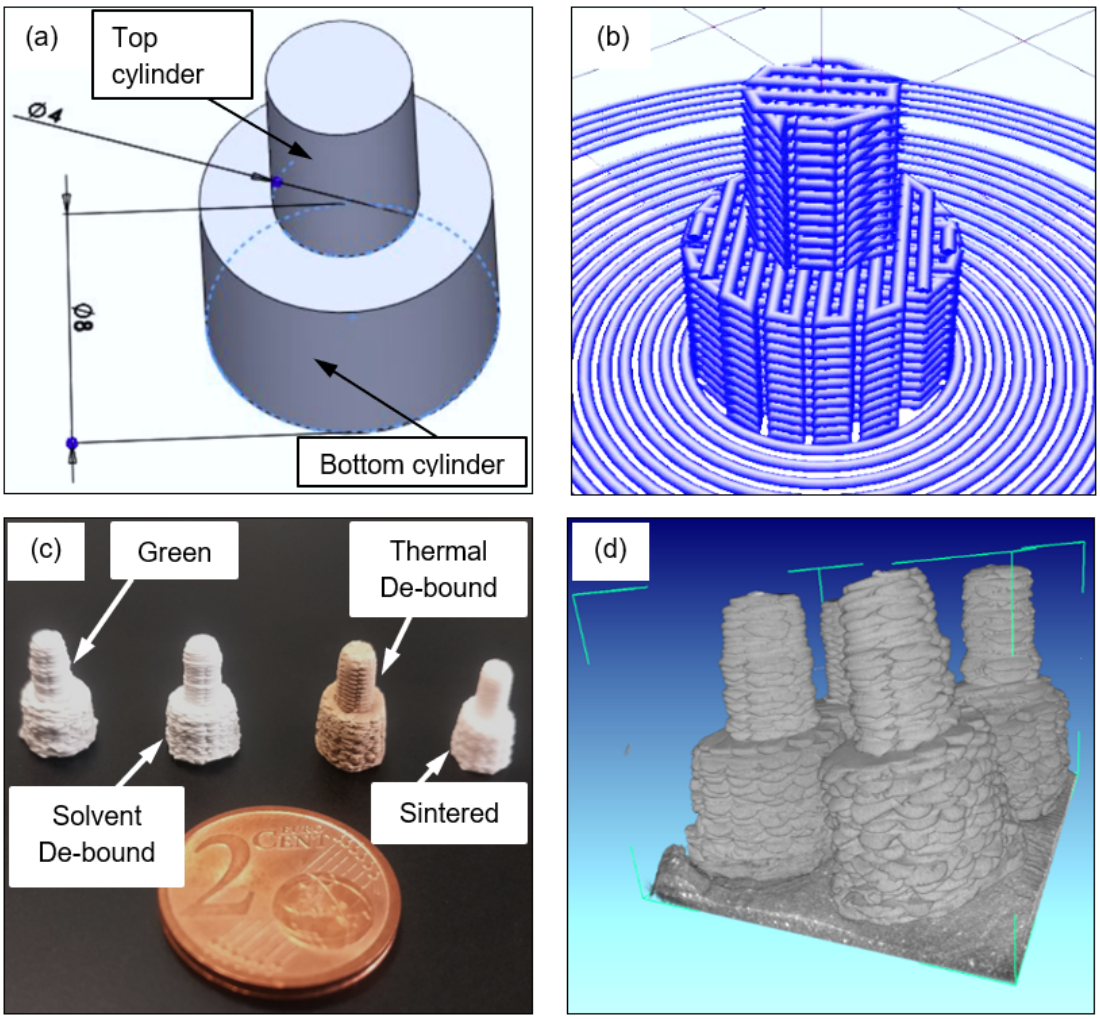

Figure 1: (a) CAD model of the double cylinder-shaped sample; (b) 3D printing roads generated by the slicer; (c) representative samples displaying colour and volume change through EAM process; (d) reconstruction of samples after CT scan using efX-CT software.

After 3D printing, the green alumina parts are processed through the two binder removal stages: solvent and thermal. A fraction of the sacrificial binder was first removed under laboratory conditions, using water as a solvent agent in an agitated water bath at 45 ^{o}C over a period of 24 hours, followed by subsequent drying at ambient conditions. Thermal de-binding was carried out in air at a temperature of 300 ^{o}C in a furnace. Complete pyrolysis of the remaining backbone binder was attained after two hours of thermal de-binding. Subsequently, sintering was carried out (at 1600 ^{o}C for a dwell time of 1 hour) in a high-temperature furnace. The implemented sintering and debinding cycle times could of course be changed. However, shorter cycle times have been tested and they lead to defective parts (cracks, excessive distrortion, uncomplete debinding). Conversely, longer cycle times would

probably improve the quality of the samples, but the would obviously generate higher manufacturing costs.

2.4 Geometry, density, and closed porosity measurements

The overall density of the 16 parts was determined by gravimetric measurements, i.e. the Archimedes' method. The measurement system consists of a precision weight scale with 0.1 mg resolution, a suspension device and a container, filled with ethanol. The measurement was repeated three times and average values of density were reported for each part. When the samples are in their final, sintered, state their bounding volume is occupied only by ceramic material or voids (i.e. there is no binder); in this case, the overall density can be used to estimate the overall volumetric porosity $P_{V\%}$ of the samples. On the contrary, when the binder is still present in the previous green and brown states, the overall density cannot be easily converted into a measure of porosity, which requires the analysis of microtomographic images.

After each experimental set reached its designated final processing stage (Figure 1 (c)), the four replicated parts belonging to the set were 3D scanned simultaneously using a micro-computed tomography machine (X25 by North Star Imaging). For each scan, 2000 2-D projections were acquired through one revolution of the rotary table. The scan volume was then reconstructed through filtered back-projection by the efX-CT software (which is the proprietary software of North Star Imaging) to create the high-resolution digital volume representations of parts as shown in Figure 1 (d). The resultant voxel size of the scans is equal to about 11.8 μm. Given the implemented image processing method, this voxel size allows the detect a void as large as a 4x4x4 set of voxels. Anything smaller would be classified as noise. After thresholding, the algorithm can detect only closed voids with an equivalent diameter larger than 47.2 μm. In order to make quantitative use of the CT scan data, it was necessary to extract slices along the Z-direction from efX-CT. The images were converted into an 8-bit format and then imported as a sequence into the ImageJ software, equipped with the BoneJ plug-in, frequently used for morphological assessment of porous materials [34]. Due to the proximity of the density of the adhesive putty used to hold the parts in place during the CT scans (see the bottom of parts in Figure 1 (d)), analyses of porosity begun from a layer height Z, safely above any putty.

Once the images were prepared, a cylindrical region of interests (ROI) was set for each of the top and bottom cylindrical portions of the parts. The diameter of the ROI was slightly smaller

than the minimum actual diameter of the part so that the ROI was completely internal to the part.

Two quantification techniques were used for porosity: a 2D porosity indicator $P_{S\%}$ and a 3D porosity indicator $P_{V\%}$. In both cases, the location of all voids was established in Cartesian coordinates X-Y-Z system and transformed into a cylindrical coordinates system r-Z. For the 2D indicator $P_{S\%}$, the image processing algorithm has been designed to detect and measure only closed voids, i.e. voids which are surrounded by solid material. This is because the study aims at characterizing the porosity generated inside the infill 3D printed roads. A distinction must be operated between porosity in the green, de-bound or sintered state.

In the green state, the porosity close to the irregular outer surface of the parts is mostly of open type, i.e. made by empty interconnected volumes, connected to the atmosphere (see Fig. 2 b). In the infill region of green samples, the porosity is mostly made of closed voids; these closed diamond-shaped voids [35] are typical of 3D printing and they are due to the deposition strategy.

During solvent de-binding, there is a mass transport phenomenon, the binder migrates outward, leaving an additional amount of both closed and open voids, also at the centre of the sample (see Fig. 2 c). The porosity is therefore expected to be larger. However, the samples are too fragile after solvent de-binding and have not been fully characterized, only a few images are available.

Finally, during thermal de-binding and sintering, shrinkage takes place, and therefore the open porosity will remain, as in the green state, only at the outer edge (see Fig. 2 d). In conclusion, at the sintered state the porosity is only closed in the infill and mostly open at the boundaries.

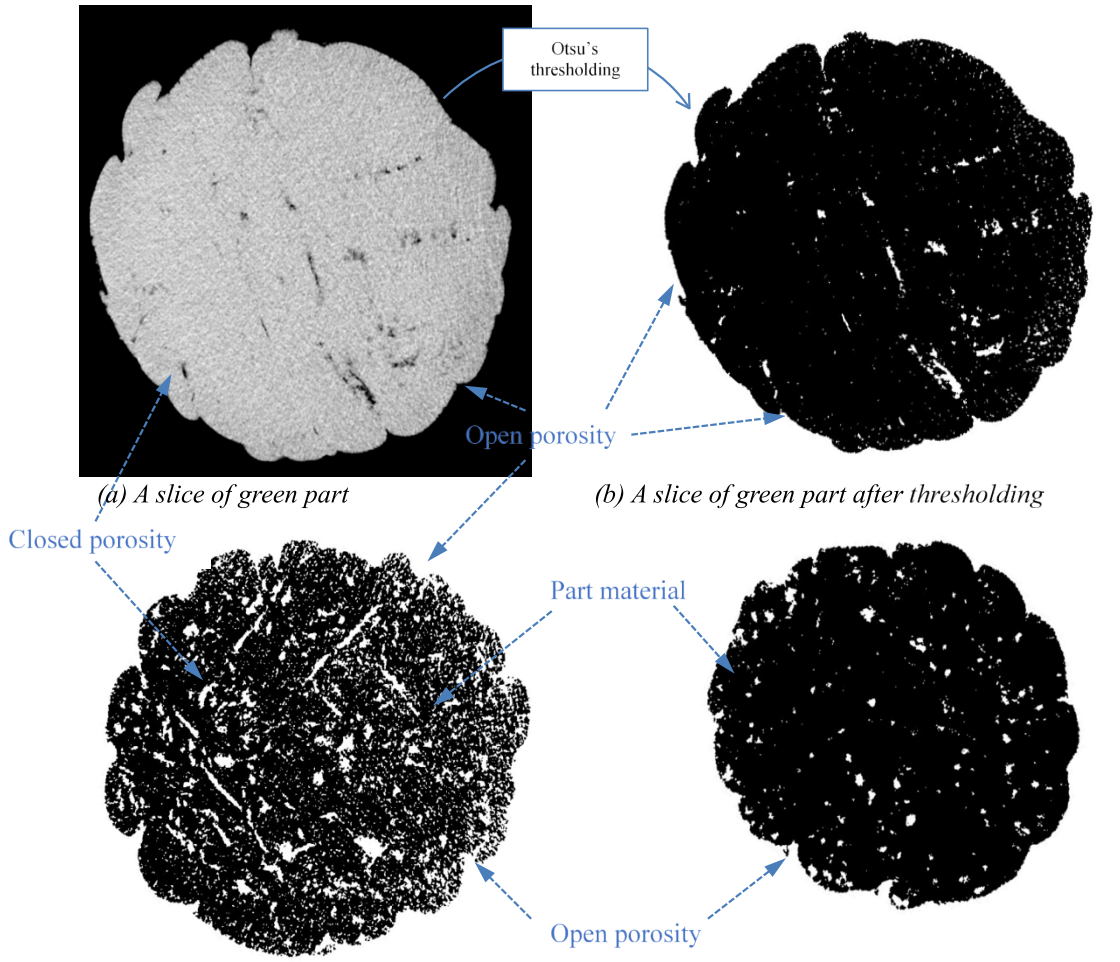

Figure 2: Method of image processing and slices showing the processing elements: Close porosity, open porosity (white) and part material (black) captured at ~2.5 mm from the bottom of the part

In the 2D assessment, the Otsu's method was applied to each slice image to estimate a binarization threshold. As an example, Figure 2 (a) has been converted into Figure 2 (b). Each individual slice along the Z-axis was evaluated by counting the pixels after thresholding. The 2D data have been used to determine the distribution of porosity along r and Z direction. The surface (2D) porosity of a given surface region of interest S was computed as the ratio $P_{S\%}=S_{void}/S$, where S_{void} is the number of white (i.e. air) pixels multiplied by the proper dimensional conversion factor, i.e. the pixel surface area. The denominator S is determined as surrounded by the outer contour of the part, built by excluding the open porosity. A representative slice of green, solvent de-bound and sintered part obtained at about 2.5 mm from the bottom are shown in Figure 2 (b), (c) and (d) respectively.

In the 3D assessment, the voids are reconstructed from the slices to form 3D entities, discretized in voxels. The 3D voxels are then computationally analysed to determine their interconnectivity in the neighbouring layers to establish the actual shape of 3D closed voids. This digital representation allows to compute the volumetric porosity of a given ROI volume V as $P_{V\%} = V_{void}/V$, where V_{void} is the number of empty voxels, multiplied by the proper dimensional conversion factor. It must be observed that $P_{V\%}$ and $P_{S\%}$ measure different dimensions, for two reasons: 1) $P_{S\%}$ is a ratio of surfaces, while $P_{V\%}$ is a ratio of volumes; 2) voids that appear closed in a 2D image might be open in the 3D reconstruction. They have been used for different purposes: $P_{S\%}$ is used to observe the radial and vertical distribution of voids; $P_{V\%}$ is used to determine the size and the morphology of voids.

The 3D reconstruction of closed voids also gives an approximation of the volume and surface area of each pore. The void morphology can be assessed through the geometrical parameters of sphericity and equivalent diameter. The centroid of all voids for each piece was determined. Sphericity is dimensionless, and its possible values lie between 0 and 1, where 1 denotes a perfect sphere. Sphericity Ψ and equivalent diameter d_{eq} of voids is determined using relations (1) and (2) respectively:

$$\Psi = \frac{\pi^{\frac{1}{3}} \times (6 \times V_p)^{\frac{2}{3}}}{A_p} \quad \text{..... (1)}$$

$$d_{eq} = 2 \times \left(\frac{3 \times V_p}{4 \times \pi}\right)^{\frac{1}{3}} \quad \text{..... (2)}$$

where: V_p = volume of the pore, A_p = surface area of the pore. d_{eq} is the diameter of a sphere of equivalent volume.

The high-resolution digital volume representations of parts have been used to determine their outer dimensions, i.e. for macroscopic geometrical metrology. The digital 3D scanned parts have been aligned with the original STL files, so that shape deviations from the designed geometry could be assessed, using the software package Cloud Compare.

The surface characteristics of the parts were captured as microscopic images using a Hitachi TM3000 Tabletop Scanning Electron Microscope.

3. Results and discussion

After following the procedure explained in Section 2.3, the porosity data were used for several analyses to quantify and map the porosity of parts through the CEAM process.

3.1 Overall density and 2D porosity measurements

The density of a sintered part is a very important parameter because it has a direct correlation to its mechanical properties. The evolution of the overall average density of alumina samples through the four CEAM process stages is shown in Figure 3 (a), as per gravimetric measurements. The figure also shows the corresponding % reduction of mass, i.e. the percentage mass loss by the part through the processing stages. Since 4 samples have been measured, Figure 3 (a) also reports error bars, calculated as the sample standard deviation. Figure 3 (a) shows that most of the mass is lost during the two de-binding stages, while most of the densification takes place during sintering, due to shrinkage.

The average density reached by the material after sintering is 3.69±0.04 g/cm³. This value is about 94% of the theoretical full density of the used ceramic material ($\rho_{Al_2O_3}$= 3.96 g/cm³). For comparison, the typical relative density of this feedstock after ceramic injection moulding and sintering is 3.8 g/cm³ (96% of the theoretical full density).

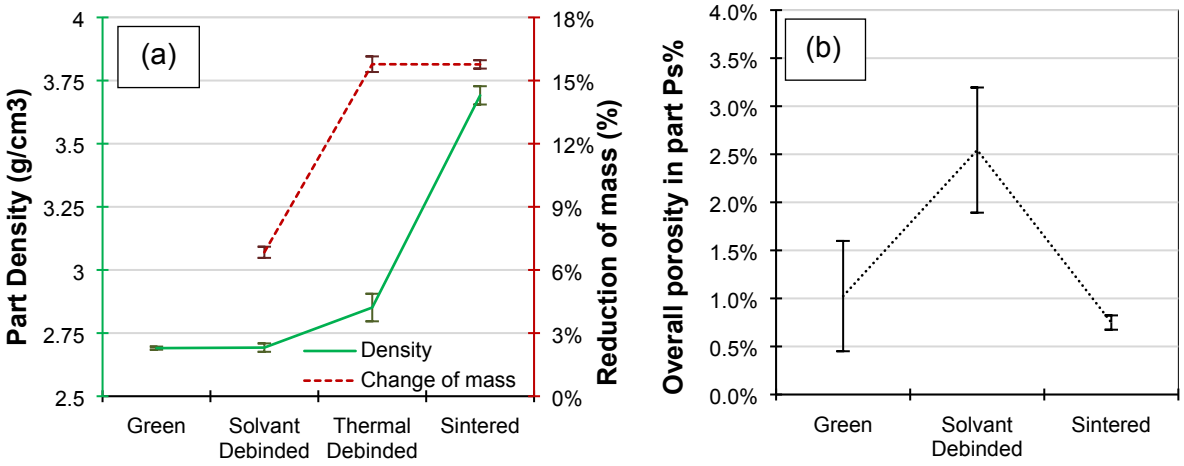

Figure 3: On density and porosity of part during CEAM (a) Evolution of density and mass loss (%) through the four process stages by gravimetric measurement; (b) evolution of closed 2D porosity $P_{s\%}$, by image analysis.

Through the CEAM process cycle, the closed porosity has been evaluated through the 2D method of image analysis described in Section 2.4. The values of overall closed porosity $P_{s\%}$ are reported in Fig. 3 (b). They have been calculated by first averaging the porosity across all slices and then by averaging the four samples tested at each stage and calculating the corresponding standard deviation. The figure shows how $P_{s\%}$ more than doubles when moving from the green state to the solvent de-bound state. This is mostly due to the binder

mass lost, as shown in Fig. 3 (a). The level of porosity after sintering is observed to be less than 1% based on the 2D analysis.

THEORETICAL INTERPRETATION OF RESULTS. The mass of samples is reduced mostly as a result of binder removal. The samples have a binder constituent (PEG) which is dissolved in water and a thermoplastic backbone which is removed by heating [36]. The weight change of the samples continues, moderately, also in the sintering stage because the residual binder left after de-binding is pyrolyzed during sintering. Despite the mass reduction, the samples densify through the process, due to a pronounced reduction of volume (shrinkage), which occurs through all stages. Shrinkage during de-binding occurs because the binder migrates outwards, and this allows the powder particles to come closer to each other. Shrinkage in thermal de-binding would be reduced with a faster heating rate [37], but this would also generate dangerous thermals stresses. Shrinkage during sintering is mostly due to solid-state diffusion of powder particles [38].

The behaviour of porosity evolution is in agreement with the known literature on the ceramic injection moulding [39]. The porosity of green samples is entirely due to the 3D printing strategy and its voids. After solvent de-binding, the voids are mostly of open type [40], i.e. continuous to the outer surface due to the mechanism of binder removal. Interconnected voids facilitate mass transport of the binders by serving as a rapid conduit for outward diffusion [20]. Because of the practical limitations of porosity evaluations after thermal de-binding, the porosity values are not available. Finally, in the sintered state the porosity is reduced to a very low value, because of the shrinkage phenomenon.

3.2 Vertical distribution of closed porosity in the part

The closed 2D porosity $P_{s\%}$ of each slice was evaluated to determine the porosity distribution with respect to the build-up direction (Z-axis) of the 3D printing. As seen in Figure 4, in the green state there is a correlation between porosity and part height (Z, μm), but only in the bottom cylinder. In the top, the values have a larger dispersion but no statistically significant trend or gradient.

The observed vertical gradient of porosity remains practically unaltered after solvent de-binding (the right part of Fig. 4), although obviously porosity increases on average because of the binder mass lost. Finally, any gradient becomes negligible after the sintering process (Figure 5).

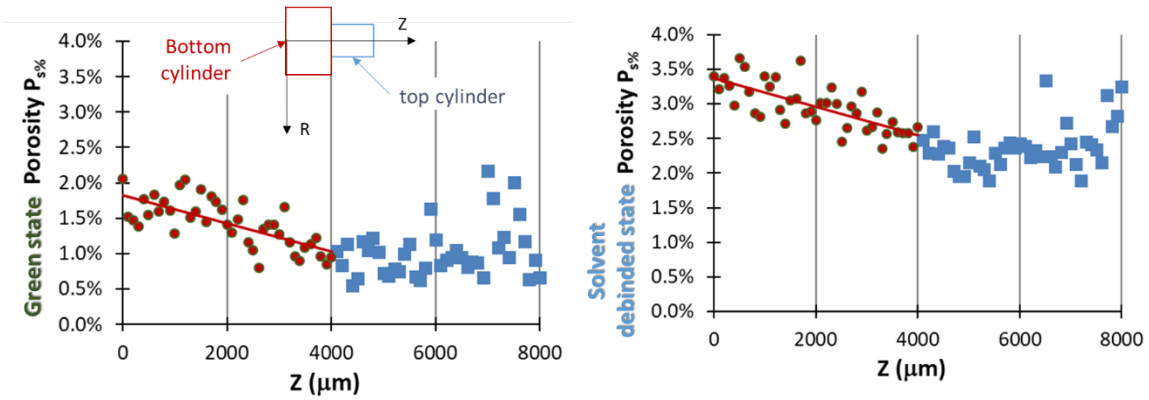

Figure 4: Evolution of closed porosity with respect to Z-axis within the two cylindrical regions of the parts in the green and solvent de-bound states.

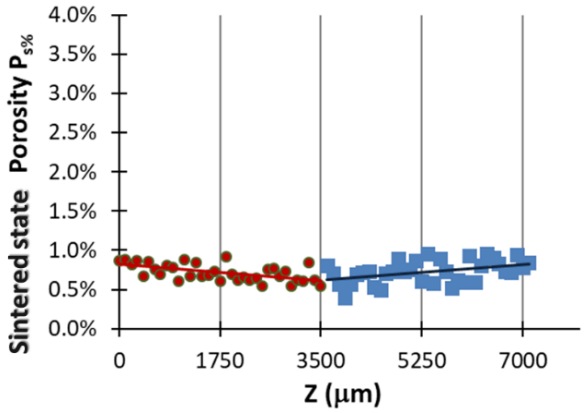

Figure 5: Evolution of closed porosity with respect to Z-axis within the two cylindrical regions of the parts at the sintered state.

EXPLANATION OF RESULTS. In the green state, each 3D printed road has a nominal layer height of 0.2 mm and is extruded out of a 0.4 mm nozzle diameter. Therefore, the deposited road will spread its width and will be much larger than 0.2 mm. In the bottom cylinder, the roads are deposited onto a stiffer base, with a smaller total deposited thickness. On the contrary, as the part height increases, each new layer is deposited over a softer and thicker substrate made of green ceramics. Consequently, the bottom roads are larger, and the top roads are smaller. In support of this explanation, it can be noted that all the 16 samples tend to have a decreasing cross-sectional area with increasing Z. In other words, the two nominally cylindrical regions are indeed slightly conical, with a larger base. This explains why the 2D porosity, which is measured in the X-Y plane, is larger for bottom layers.

In the solvent and thermal de-binding stages, the binder removal process is through mass transport and is dependent on the mass, on the surface area and on the geometrical modulus

of the part (volume-to-surface ratio). A smaller part of modulus should facilitate de-binding [20]. However, a comparison between the green and de-bound states shows that the gradients are unaltered by the de-binding process. Porosity increases in de-binding because of the binder removal, but the distribution of porosity induced in the green parts maintains its trend. In other words, the vertical porosity distribution is mostly generated and due to the 3D printing process and the geometrical modulus of the parts has no effect on the vertical gradient.

Finally, any vertical porosity gradient disappears after sintering. In Section 3.2 it is demonstrated that shrinkage reduces porosity and increases density. The forces that pull together the powder particles during the sintering process can close (although not completely) the voids induced by 3D printing and left by the removed binder. While the number and size of voids decreases, the shrinkage phenomenon acts as a regularization process and reduces the porosity gradient.

3.3. Radial distribution of closed porosity $P_{s\%}$

In order to obtain a radial distribution of porosity, each closed void in the 2D space has been associated with a radial coordinate *r*. Each slice has been segmented into 8 annular regions with increasing r-value. For each of the 8 annular regions, a local porosity value has been calculated and averaged across all available slices of the bottom cylinder (where porosity is larger).

The result is plotted in Figure 6, with increasing depth (*R*-*r*) from the part surface, where *R* is the overall radius of the part. The grand average of closed porosity for each of the different states is represented by the dashed line in the plots.

The shape of the three radial profiles (green, solvent de-bound, and sintered) are indeed very peculiar and similar to each other. They all have a maximum of closed porosity at around halfway between the centre and the boundary (when R-r = 2000 μm). The closed porosity decreases in the left part of all diagrams, because close to the outer boundary most of the voids are interconnected, i.e. open, and are not included in the $P_{s\%}$ indicator. More noticeably, the porosity decreases as we move from a radial distance of 2000 μm towards the centre of the samples (at around 4000 μm for green and solvent de-bound parts, whereas at around 3250 μm for the sintered part).

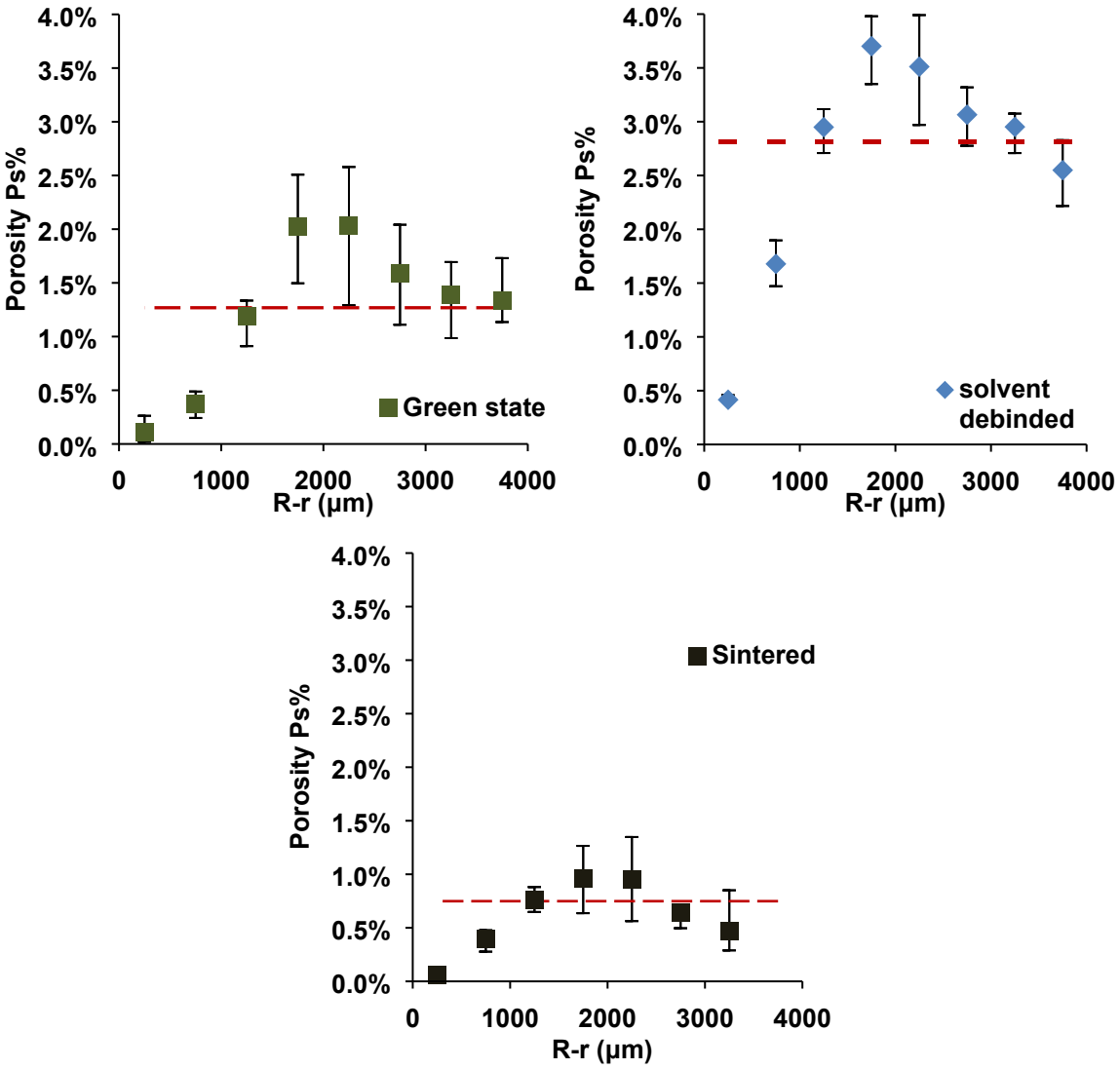

Figure 6: Evolution of closed porosity $P_{s\%}$ with respect to R-r in the bottom cylindrical region of the parts; the centre of the samples is where R-r=4000 µm.

After solvent de-binding, as already observed for the vertical gradient, the radial gradient does not change its shape.

After sintering, the porosity is significantly reduced, with an average value below 1%, but the shape of the porosity profile is still very similar to the profile observed in the green state. In the sintered samples, the closed porosity towards the centre is smaller than 0.5%.

EXPLANATION OF RESULTS. The closed-cell porosity is smaller at the heart of the samples, at all states. In the green state, this is because the deposited material is more compacted, compressed at the centre, hence the voids are smaller. In the de-bound and sintered states, the radial gradient does not decrease because the binder migrates radially, and the binder located

at the centre of the samples is more difficult (slower) to be removed. This is also why, in binder removal processes, there is a maximum limit for wall thickness [41] of samples. It is therefore reasonable that the closed porosity progressively increases moving radially towards the outer surface. However, the trends in Fig 6 exhibit s maximum, i.e. the closed porosity dramatically decreases and nearly vanishes when approaching the outer surface of the samples. The reason is that the porosity becomes progressively more open, i.e. connected to the air and it is therefore undetected by the $P_{s\%}$ indicator.

3.4. Void size and shape distribution in the part

To characterize the individual voids and their evolution through CEAM process, their 3D morphology has been assessed by 3D image analysis at the different states. The sphericity Ψ and the equivalent spherical diameter d_{eq} were determined from the obtained volume and surface area of each closed void. The results are effectively reported in Figure 7, where all measured voids of all samples are shown on the same plot at the green, solvent de-bound, and sintered states. Their distribution within each stage is considerably scattered.

The three clouds of points are significantly different. In the green state, diameter and sphericity of voids are strongly negatively correlated, i.e. larger voids are less spherical. A negative exponential trendline is plotted in the diagram, along with a marker that represents the average of all values. Void size and shape are significantly scattered over a large range.

After solvent de-binding, the void shapes and sizes are further scattered because the binder volume is partially replaced by voids. For the same reason, the negative correlation between d_{eq} and Ψ weakens.

While Figure 7 reports all voids detected in all samples at a given process state, Figure 8 provides a representation of the spatial distribution of void shape (sphericity Ψ) in cylindrical coordinates for each state. The contour plots have been created in MATLAB, performing some interpolations. Some portions of the shape had to be trimmed away because of a very large interpolation error. Therefore, the quarter cross-sectional profile in Figure 8 does not appear like the cross-section of a double cylindrical piece. Despite the figures are odd and do not fully map the morphology across the cross-section, they still very clearly show a strong correlation of sphericity with respect to the vertical Z-axis. At the green state, the value of sphericity is 0.4 near the bottom and nearly 0.6 at the top.

Similar contour maps could be plotted for the equivalent diameter, but they are omitted because they would not show any clear spatial correlation of void size with increasing height Z nor radius r.

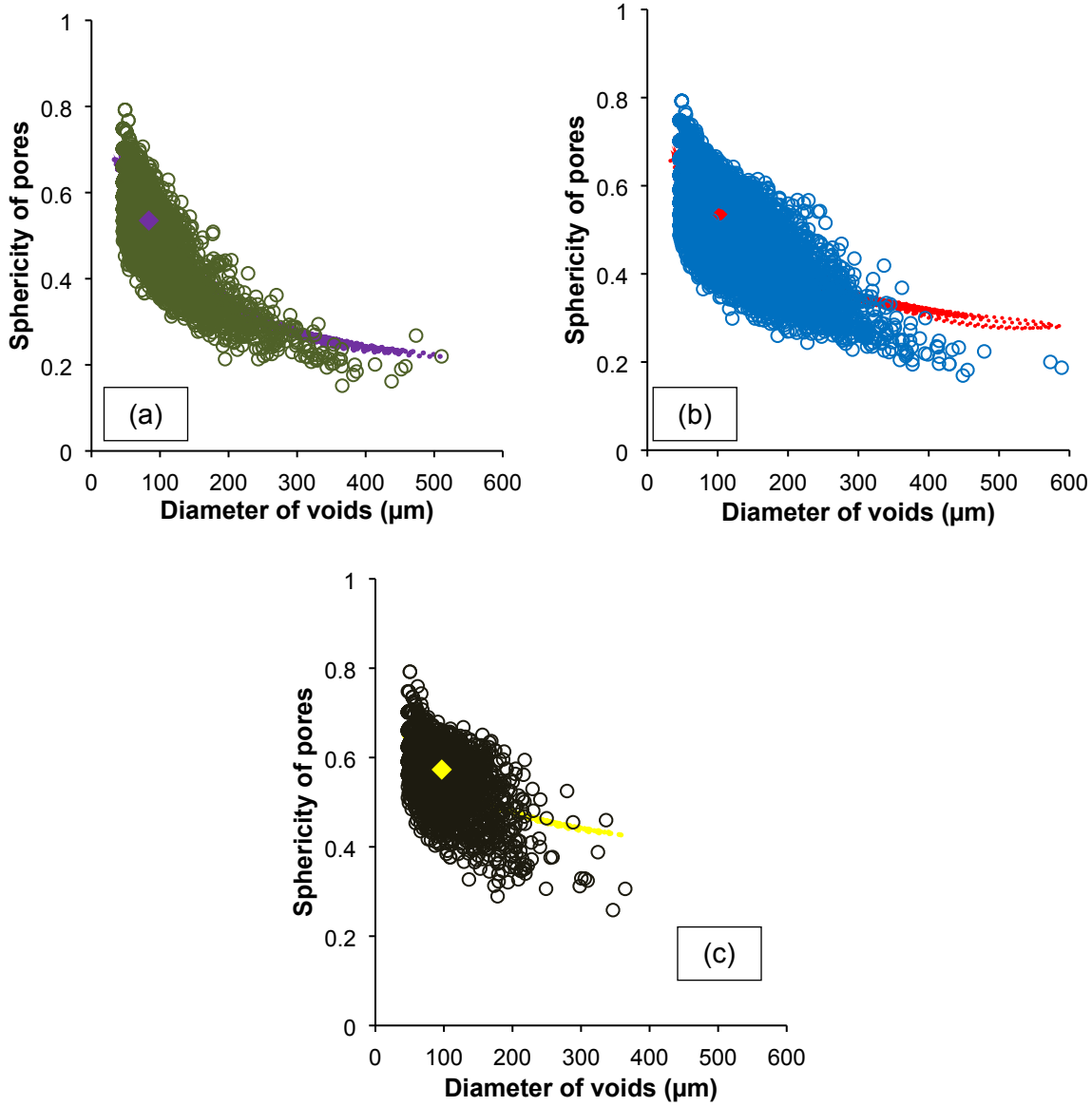

Figure 7: Evolution of void sphericity Ψ vs. diameter d_{eq} during EAM process states: (a) green (b) solvent de-bound and (c) sintered; the diamond symbol represents the average values; the dotted line represents a negative exponential trendline.

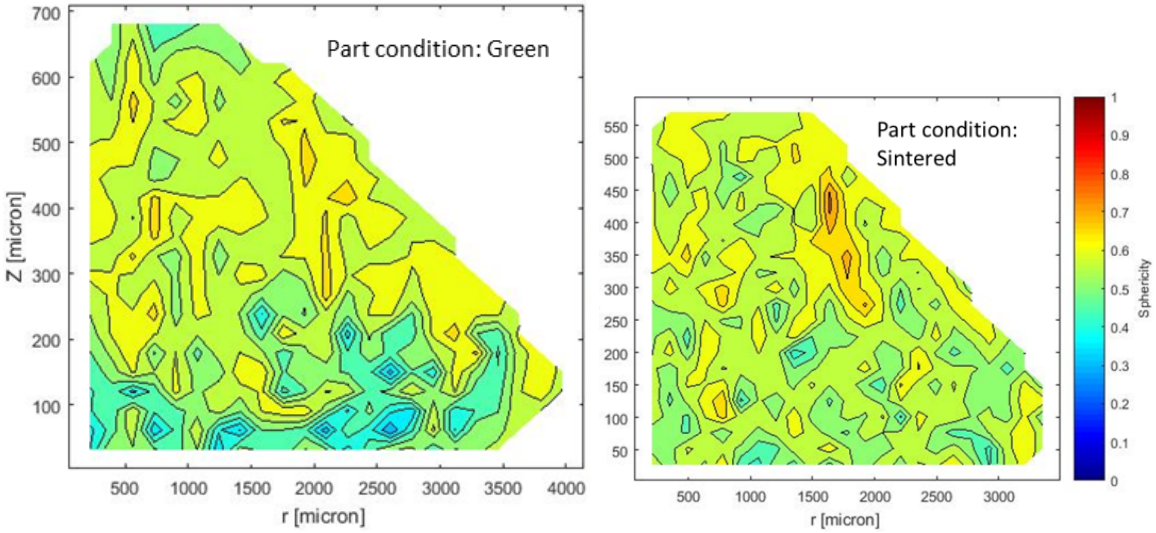

Figure 8: Contour plots of the distribution of void sphericity within an EAM part in the green and sintered state as a function of sample height Z and radius r.

EXPLANATION OF RESULTS. The morphological analysis shows that, in all stages, there is a negative exponential correlation between sphericity and equivalent diameter of voids. In other words, smaller

voids are more spherical, while larger voids are less spherical. This behaviour has been observed before for sintered materials [42], but the present study shows that it is even more evident at the green state, i.e. before sintering. A possible explanation is that large voids, which are produced by the uncomplete filling of the 3D printed roads, tend to have a diamond-like non spherical surface. On the contrary, smaller voids, which are due to local random inhomogeneities in the feedstock mixture, tend to be spherical.

Another interesting observation is that the voids are less spherical at the bottom cylinder. This agrees with the previous remarks on the vertical porosity distribution, which is larger at the bottom of the green samples. As already stated, vois at the bottom are larger and, therefore, less spherical.

3.5. Geometrical variations during CEAM

The linear deviations in green and de-bound parts with respect to their nominal dimensions were determined by overlapping the 3D volumetric representation of parts in each stage with the corresponding CAD model (Table 2). The green and de-bound parts have been compared to the CAD model used in 3D printing. The dimensional deviations in the green part are due to several causes, including discretization errors due to the slicing process. The data in Table

2 also indicate that there are no major geometrical changes that occur in the de-binding stages, as already shown by the density evolution in Figure 3.

Table 2: Cumulative deviation in part dimensions through CEAM process

Process stage	Green (After 3D printing)	After solvent de-binding	After thermal de-binding	After sintering
Mean linear deviation (mm) from the green CAD model	-0.37	-0.31	-0.32	-0.63
Mean linear deviation (mm) from the sintered CAD model	n.a.	n.a.	n.a.	-0.22
Standard deviation (mm)	0.25	0.27	0.26	0.19

The sintered parts have also been compared to a CAD model computed by shrinking the 3D printing CAD model by 15.5% on linear dimensions, which is the nominal predicted value for this feedstock. Indeed, the sintered parts had a measured linear shrinkage after sintering of 13.4%, with respect to the green part dimensions. Figure 9 shows the deviation of sintered parts from their nominal dimensions. The deviations are due to: 3D printing errors, error in predicting the linear shrinkage, distortions. Interestingly, the top regions of the parts have larger final deviations.

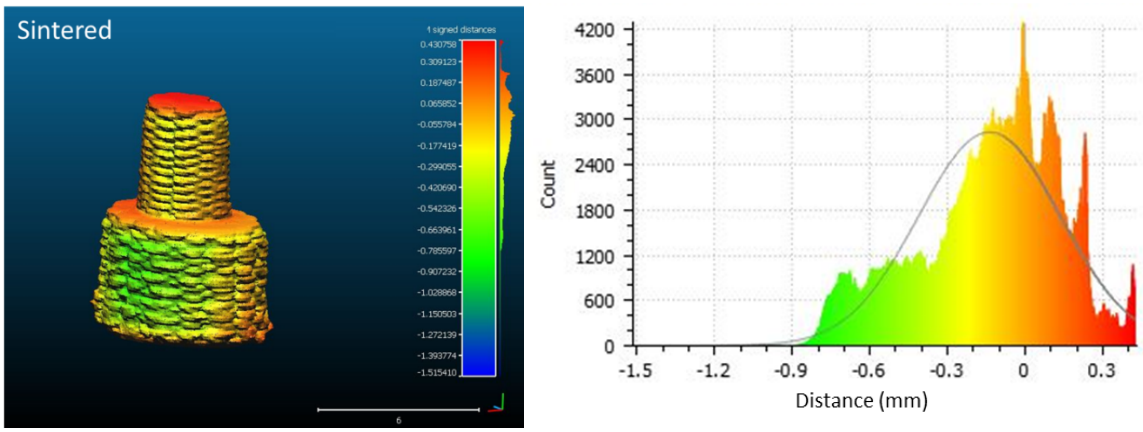

Figure 9: Dimensional deviation of sintered parts with respect to the CAD model

3.6. Effect of the part state on surface quality

Figure 10 shows the magnified side views of 3D printed parts. Since all parts have been deposited with no contour, the outer surfaces are quite irregular both in the green and sintered states. Furthermore, there is excess material at each direction reversals of roads, because of

the deceleration of the table at the direction changes. However, the micrographs indicate that, with respect to the green state, the surface irregularities in sintered parts are significantly smaller, due to shrinkage. It is also noticeable that micro-cracks are visible in the green state, in Figure 10 (a), and they remain in the sintered state.

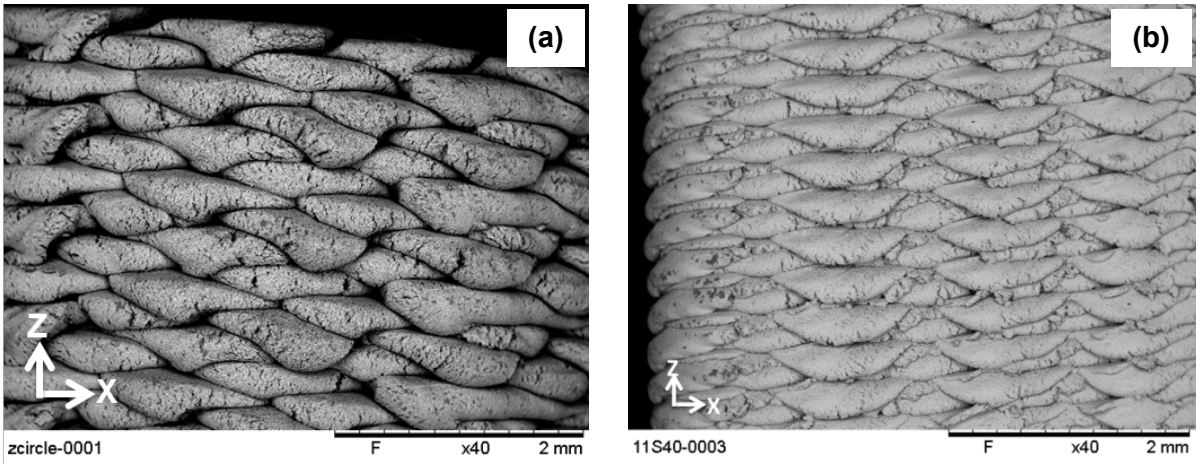

Figure 10: SEM micrographs of (a) green and (b) sintered alumina parts

4. Conclusions

In this work, alumina samples shaped as double-diameter pins parts were produced through the stages of the Ceramic Extrusion Additive Manufacturing process: 3D printing, solvent de-binding, thermal de-binding, and sintering.

The final average mass reduction was 16%; most of the mass was lost during the two de-binding phases. The final relative density was 94%; most of the densification took place during sintering. The final overall surface (i.e. layer-wise) porosity was less than 1%, after sintering.

A vertical gradient of porosity is present in green and de-bound samples, with porosity decreasing with increasing sample height. This is mainly due to mechanics of the 3D printing process, because the roads of the first 3D printed layers, which are closer to the build platform, are wider. After sintering, the vertical gradient of porosity disappears, due to the strong material shrinkage that acts as a homogenization mechanism.

A minor radial gradient of closed porosity is also present in the first two states, and it is also strongly reduced after sintering. The closed porosity is smaller at the centre of samples. On the contrary, open-cell porosity is mainly present closed to the outer surface.

From a morphological point of view, the sphericity and the diameter of voids are negatively correlated and dispersed over a wide range in the green state. Conversely, the equivalent diameter and the sphericity of voids are less dispersed and less correlated, i.e. more uniformly distributed, after sintering. Furthermore, there is a correlation of sphericity with respect to the vertical direction. At the green state, voids which are closer to the bottom of samples are less spherical and larger. Again, the sintering process has a homogenization effect on the void shape distribution.

Finally, both the geometrical deviation and the surface quality of parts improves when moving from the green to the sintered state.

Acknowledgments

Authors are thankful to Mr. Guillaume Herve of Politecnico di Milano and Mr. Valerio Mussi of the MUSP research lab (www.musp.it) of Piacenza (Italy), for their precious help in the image analysis and sintering operations respectively.

References

[1] O. Santoliquido, P. Colombo, A. Ortona, Additive Manufacturing of ceramic components by Digital Light Processing: A comparison between the "bottom-up" and the "top-down" approaches, J. Eur. Ceram. Soc. (2019) 0–1. doi:10.1016/J.JEURCERAMSOC.2019.01.044.

[2] G. Mitteramskogler, R. Gmeiner, R. Felzmann, S. Gruber, C. Hofstetter, J. Stampfl, J. Ebert, W. Wachter, J. Laubersheimer, Light curing strategies for lithography-based additive manufacturing of customized ceramics, Addit. Manuf. 1 (2014) 110–118. doi:10.1016/j.addma.2014.08.003.

[3] S.L. Sing, W.Y. Yeong, F.E. Wiria, B.Y. Tay, Z. Zhao, L. Zhao, Z. Tian, S. Yang, Direct selective laser sintering and melting of ceramics: A review, Rapid Prototyp. J. 23 (2017) 611–623. doi:10.1108/RPJ-11-2015-0178.

[4] J.A. Gonzalez, J. Mireles, Y. Lin, R.B. Wicker, Characterization of ceramic components fabricated using binder jetting additive manufacturing technology, Ceram. Int. 42 (2015) 10559–10564. doi:10.1016/j.ceramint.2016.03.079.

[5] J. Deckers, J. Vleugels, J.P. Kruth, Additive manufacturing of ceramics: A review, J. Ceram. Sci. Technol. 5 (2014) 245–260. doi:10.4416/JCST2014-00032.

[6] J. Gonzalez-Gutierrez, S. Cano, S. Schuschnigg, C. Kukla, J. Sapkota, C. Holzer, Additive Manufacturing of Metallic and Ceramic Components by the Material Extrusion of Highly-Filled Polymers: A Review and Future Perspectives, Materials (Basel). 11 (2018) 840. doi:10.3390/ma11050840.

[7] P. Parenti, S. Cataldo, M. Annoni, Shape deposition manufacturing of 316L parts via feedstock extrusion and green-state milling, Manuf. Lett. 18 (2018) 6–11.

doi:10.1016/j.mfglet.2018.09.003.

[8] K. Rane, L. Di Landro, M. Strano, Processability of SS316L powder - binder mixtures for vertical extrusion and deposition on table tests, Powder Technol. 345 (2019) 553–562. doi:10.1016/j.powtec.2019.01.010.

[9] A. Bellini, L. Shor, S.I. Guceri, New developments in fused deposition modeling of ceramics, Rapid Prototyp. J. 11 (2005) 214–220. doi:10.1108/13552540510612901.

[10] M. Annoni, H. Giberti, M. Strano, Feasibility Study of an Extrusion-based Direct Metal Additive Manufacturing Technique, Procedia Manuf. 5 (2016) 916–927. doi:10.1016/j.promfg.2016.08.079.

[11] S. Cano, J. Gonzalez-Gutierrez, J. Sapkota, M. Spoerk, F. Arbeiter, S. Schuschnigg, C. Holzer, C. Kukla, Additive manufacturing of zirconia parts by fused filament fabrication and solvent debinding: Selection of binder formulation, Addit. Manuf. 26 (2019) 117–128. doi:10.1016/j.addma.2019.01.001.

[12] F. Mohd Foudzi, N. Muhamad, A. Bakar Sulong, H. Zakaria, Yttria stabilized zirconia formed by micro ceramic injection molding: Rheological properties and debinding effects on the sintered part, Ceram. Int. 39 (2013) 2665–2674. doi:10.1016/j.ceramint.2012.09.033.

[13] S. Tang, L. Yang, G. Li, X. Liu, Z. Fan, 3D printing of highly-loaded slurries via layered extrusion forming: Parameters optimization and control, Addit. Manuf. 28 (2019) 546–553. doi:10.1016/j.addma.2019.05.034.

[14] I. Grida, J.R.G. Evans, Extrusion freeforming of ceramics through fine nozzles, J. Eur. Ceram. Soc. 23 (2003) 629–635. doi:10.1016/S0955-2219(02)00163-2.

[15] H. Giberti, M. Strano, M. Annoni, An innovative machine for Fused Deposition Modeling of metals and advanced ceramics, in: MATEC Web Conf., Les Ulis, 2016: p. 3003. doi:10.1051/mateccont/20164303003.

[16] L. Yang, H. Miyanaji, Ceramic Additive Manufacturing: a review of current status and challenges, in: Proc. 28th Annu. Int. Solid Free. Fabr. Symp., Austin (TX), 2017: pp. 652–679.

[17] R.J. Zaldivar, D.B. Witkin, T. McLouth, D.N. Patel, K. Schmitt, J.P. Nokes, Influence of processing and orientation print effects on the mechanical and thermal behavior of 3D-Printed ULTEM ® 9085 Material, Addit. Manuf. 13 (2017) 71–80. doi:10.1016/j.addma.2016.11.007.

[18] K. Okada, T. Tomita, A. Nakajima, T. Isobe, Y. Kameshima, Preparation and properties of porous alumina ceramics with oriented cylindrical pores produced by an extrusion method, J. Eur. Ceram. Soc. 26 (2005) 957–960. doi:10.1016/j.jeurceramsoc.2004.11.015.

[19] Y.W. Moon, K.H. Shin, Y.H. Koh, W.Y. Choi, H.E. Kim, Production of highly aligned porous alumina ceramics by extruding frozen alumina/camphene body, J. Eur. Ceram. Soc. 31 (2011) 1945–1950. doi:10.1016/j.jeurceramsoc.2011.04.033.

[20] W.J. Tseng, C.-K. Hsu, Cracking defect and porosity evolution during thermal debinding in ceramic injection moldings, Ceram. Int. 25 (1999) 461–466.

doi:10.1016/S0272-8842(98)00061-3.

[21] S.J. Kalita, S. Bose, H.L. Hosick, A. Bandyopadhyay, Development of controlled porosity polymer-ceramic composite scaffolds via fused deposition modeling, Mater. Sci. Eng. C. 23 (2003) 611–620. doi:10.1016/S0928-4931(03)00052-3.

[22] S.X. Zhang, Z.Y. Ong, T. Li, Q.F. Li, S.F. Pook, Ceramic composite components with gradient porosity by powder injection moulding, Mater. Des. 31 (2010) 2897–2903. doi:10.1016/j.matdes.2009.12.030.

[23] L. Olmos, T. Takahashi, D. Bouvard, C.L. Martin, L. Salvo, D. Bellet, M. Di Michiel, Analysing the sintering of heterogeneous powder structures by in situ microtomography, Philos. Mag. 89 (2009) 2949–2965. doi:10.1080/14786430903150225.

[24] S. Iyer, J. Mcintosh, A. Bandyopadhyay, N. Langrana, A. Safari, S.C. Danforth, R.B. Clancy, C. Gasdaska, P.J. Whalen, Microstructural Characterization and Mechanical Properties of Si3N4 Formed by Fused Deposition of Ceramics, Int. J. Appl. Ceram. Technol. 5 (2008) 127–137. doi:10.1111/j.1744-7402.2008.02193.x.

[25] L.M. Anovitz, D.R. Cole, Characterization and Analysis of Porosity and Pore Structures, Rev. Mineral. Geochemistry. 80 (2015) 61–164. doi:10.2138/rmg.2015.80.04.

[26] S. Cacace, A.G. Demir, Q. Semeraro, Densification Mechanism for Different Types of Stainless Steel Powders in Selective Laser Melting, Procedia CIRP. 62 (2017) 475–480. doi:10.1016/j.procir.2016.06.010.

[27] W. Dewulf, M. Pavan, T. Craeghs, J.-P. Kruth, Using X-ray computed tomography to improve the porosity level of polyamide-12 laser sintered parts, CIRP Ann. 65 (2016) 205–208. doi:10.1016/j.cirp.2016.04.056.

[28] H. Taud, R. Martinez-Angeles, J.F. Parrot, L. Hernandez-Escobedo, Porosity estimation method by X-ray computed tomography, J. Pet. Sci. Eng. 47 (2005) 209–217. doi:10.1016/j.petrol.2005.03.009.

[29] D. Cooper, A. Turinsky, C. Sensen, B. Hallgrimsson, Effect of voxel size on 3D micro-CT analysis of cortical bone porosity, Calcif. Tissue Int. 80 (2007) 211–219. doi:10.1007/s00223-005-0274-6.

[30] M. Freire-Gormaly, J.S. Ellis, A. Bazylak, H.L. MacLean, Comparing thresholding techniques for quantifying the dual porosity of Indiana Limestone and Pink Dolomite, Microporous Mesoporous Mater. 207 (2015) 84–89. doi:10.1016/j.micromeso.2015.01.002.

[31] M. Monno, D. Negri, V. Mussi, P. Aghaei, G. Groppi, E. Tronconi, M. Strano, Cost-Efficient Aluminum Open-Cell Foams: Manufacture, Characterization, and Heat Transfer Measurements, Adv. Eng. Mater. 20 (2018) 1701032. doi:10.1002/adem.201701032.

[32] S. Mitra, M. El, Micro-focus X-Ray Computed Tomography (CT) Analysis of functional 3D Printed sand mold, in: Procedia Manuf. - NAMRC 47, Erie, PA (USA), 2019.

[33] H. Giberti, L. Sbaglia, M. Silvestri, Mechatronic Design for an Extrusion-Based Additive Manufacturing Machine, Machines. 5 (2017) 29. doi:10.3390/machines5040029.

[34] M.J. Mirzaali, V. Mussi, P. Vena, F. Libonati, L. Vergani, M. Strano, Mimicking the loading adaptation of bone microstructure with aluminum foams, Mater. Des. 126 (2017) 207–218. doi:10.1016/j.matdes.2017.04.039.

[35] J.F. Rodriguez, J.P. Thomas, J.E. Renaud, Characterization of the mesostructure of fused-deposition acrylonitrile-butadiene-styrene materials, Rapid Prototyp. J. 6 (2000) 175–186. doi:10.1108/13552540010337056.

[36] K. Sharmin, I. Schoegl, Optimization of binder removal for ceramic microfabrication via polymer co-extrusion, Ceram. Int. 40 (2014) 3939–3946. doi:10.1016/j.ceramint.2013.08.039.

[37] N.H. Loh, R.M. German, Statistical analysis of shrinkage variation for powder injection molding, J. Mater. Process. Technol. 59 (1996) 278–284. doi:10.1016/0924-0136(95)02158-2.

[38] M. Sahli, A. Lebied, J.C. Gelin, T. Barrière, B. Necib, Numerical simulation and experimental analysis of solid-state sintering response of 316 L stainless steel micro-parts manufactured by metal injection molding, Int. J. Adv. Manuf. Technol. 79 (2015) 2079–2092. doi:10.1007/s00170-015-6983-8.

[39] R.V.B. Oliveira, V. Soldi, M.C. Fredel, A.T.N. Pires, Ceramic injection moulding: influence of specimen dimensions and temperature on solvent debinding kinetics, J. Mater. Process. Technol. 160 (2005) 213–220. doi:10.1016/j.jmatprotec.2004.06.008.

[40] M. Trunec, J. Cihlar, Thermal removal of multicomponent binder from ceramic injection mouldings, J. Eur. Ceram. Soc. 22 (2002) 2231–2241. doi:10.1016/S0955-2219(02)00015-8.

[41] S. Banerjee, C.J. Joens, Debinding and sintering of metal injection molding (MIM) components, in: D.F. Heaney (Ed.), Handb. Met. Inject. Molding, Elsevier, 2019: pp. 129–171. doi:10.1016/B978-0-08-102152-1.00009-X.

[42] N. Chawla, X. Deng, Microstructure and mechanical behavior of porous sintered steels, Mater. Sci. Eng. A. 390 (2005) 98–112. doi:10.1016/j.msea.2004.08.046.